High speed stereo-vision study of laminated glass fragmentation upon impact

Corentin Le Gourriérec, Xuyang Chang, Bastien Durand, Richard Villey, Benoît Voillot, Xavier Brajer, Stéphane Roux

High speed stereo-vision study of laminated glass fragmentation upon impact

Corentin Le Gourriérec[a,b,*], Xuyang Chang[a], Bastien Durand[a], Richard Villey[c], Benoît Voillot[b], Xavier Brajer[b], Stéphane Roux[a]

[a] *Université Paris-Saclay, CentraleSupélec, ENS Paris-Saclay, CNRS, LMPS - Laboratoire de Mécanique Paris-Saclay, 4 Avenue des Sciences, Gif-sur-Yvette, 91190, France*
[b] *Saint-Gobain Research Paris, 39 Quai Lucien Lefranc, Aubervilliers, 93300, France*
[c] *Saint-Gobain Research Compiègne, 1 rue de Montluçon, Thourotte, 60150, France*

Abstract

The different stages of an impact on laminated glass are difficult to observe and quantify but are essential for numerical model validation. To assess the performance of this composite to low-velocity (∼10 m/s) high-mass impacts, dynamical impact tests, inspired by ball-drop tests, are performed, equipped with multiple high-speed cameras. From the set of images, a continuous 3D shape reconstruction of the deformed laminated glass over time is performed using Stereo-Digital Image Correlation (S-DIC). Significant brightness and contrast variations captured by two cameras due to large rotations of glass fragments and large strain of the polymer interlayer between fragments render

*Corresponding author
Email addresses: corentin.legourrierec@saint-gobain.com (Corentin Le Gourriérec), xuyang.chang@ens-paris-saclay.fr (Xuyang Chang), bastien.durand@ens-paris-saclay.fr (Bastien Durand), richard.villey@saint-gobain.com (Richard Villey), benoit.voillot@saint-gobain.com (Benoît Voillot), xavier.brajer@saint-gobain.com (Xavier Brajer), stephane.roux@ens-paris-saclay.fr (Stéphane Roux)

the use of S-DIC difficult as the impactor penetrates deeper into the plate. To circumvent this problem, an axisymmetric regularization is introduced which has the advantage of not requiring prior knowledge of the mechanical behavior for the tested specimen. It is shown that it offers a more extended period of time (as compared to regular S-DIC) over which a trustful analysis can be performed. The time evolution of the fragmented laminated glass and the density of cracks, both available from our analysis, are key ingredients to elaborate quantitative modeling of the dynamic performance of the laminate.
Keywords: stereo-Digital Image Correlation, stereo-vision, laminated glass, low-velocity impact, hard-body impact.

Acknowledgments

The authors would like to thank Saint-Gobain Research, Saint-Gobain Research Compiègne and ENS Paris-Saclay for helping carrying out the *cannon* experiments. Many thanks to Maxime Da Rocha for conducting the *cannon* tests. We acknowledge interesting suggestions and discussions with René Gy, François Hild and Keyvan Piroird. This project was funded by ANRT (CIFRE 2019/0676) and Saint-Gobain.

Declaration of Competing Interest

The authors declare that they have no known competing interests.

Authors contribution

All authors planned the experiments, the experimental strategy and discussed the results. CLG, RV, BV carried out the experiments. CLG per-

formed the S-DIC measurements with Correli 3.0 and implemented the axisymmetric regularization. XC implemented and performed the numerical calibration of the stereo-vision system. CLG, SR, XC, BD, RV wrote the paper.

1. Introduction

Laminated glass, a composite made of two or more different glass sheets interleaved with thin polymeric layers, is widely used for building or automotive applications. It has been engineered to meet a wide range of demanding properties: transparency, stiffness, low weight, acoustic insulation, and, most importantly, its ability to ensure the safety of people upon shocks or impacts due to the residual resistance offered by the polymeric layers following the fracture of the glass sheets. Therefore, research topics in the resistance to impacts focus on the designing of new laminated glass plates while respecting the criteria of personal protection, which remains the major characteristic of such glazing. Characterizing and quantifying the mechanical response of laminated glass during a low-velocity impact, especially structural degradation and integrity is a critical issue for manufacturers of laminated glass, who must validate certain norms to sell their production (European Norm 2000; 2003). Such impacts can be met when a pedestrian is hit by a car (Chen et al. 2016), when people fall from their height onto a laminated glazing (Huang et al. 2023), or if hand tools are used for a burglary (Schuster et al. 2020), for instance. Each of these loading cases has a velocity in the 1 to 10 m/s range. During such dynamic load, just after contact, cracks are initiated and propagated in the glass plies. Thanks to a finely adjusted adhesion between glass and polymer interlayer, with large stretching capacity and toughness (Martìn et al. 2020) – for example made of polyvinyl butyral (PVB) –, the newly-fragmented plate can accomodate large out-of-plane displacements via the glass fragments delamination from the stretched membrane, dissipating a large amount of the energy. Adhesion between the layers is also tuned –

regarding the polymer layer thickness – to prevent large splinters from detaching then causing injuries, and avoid projectile penetration through the structure (Pelfrene et al. 2016).

During a typical fragmentation test with the *cannon* (Nourry 2005), the half-sphere apex impacts the glass surface at that initial velocity v_0 and with a normal incidence. In the first microseconds after impact, the laminate behaves elastically for the most part, while a small zone of the first ply right under the impactor head is crushed under intense multiaxial loading. Depending on the impact velocity and the sample strength, the first radial cracks may appear from the plate center within a few microseconds to a few hundreds of microseconds. As the plate bends, the radial cracks extend and sometimes become more numerous, while orthoradial cracks are also formed. More and more cracks are created during the whole impact duration. When the fragmentation is well-advanced, the stretching (and possibly tearing out) of the PVB interlayer dissipates a large amount of the impact energy as the impactor stroke increases. This dissipation occurs at the PVB bridge locations that connect all the glass fragments (Seshadri et al. 2002). The initial projectile velocity plays an important role in the laminated glass behavior to impact. Two failure modes can be distinguished as introduced by Li et al. (Li et al. 2023): the *punching failure* which involves intense shear loading in the membrane structure of a densely fragmented plate, and the *bending failure* with fewer cracks formed and much more bending energy stored in the glass – in compression – and in the interlayer – in tension (Li et al. 2023).

Many experimental studies have been carried out to better understand the mechanics of laminated glass under impact. Particularly, the semi-

rigid or head-form impact on windshields is at stake: Yu et al. tested different locations on windshields and analyzed the impact acceleration versus the crack pattern evolution on the fragmented plate (Yu et al. 2017). Yunqi Li et al. compared soda-lime and tempered glass performances (Li et al. 2019). Dong Li et al studied the dissymmetry of the glass layers regarding impact performances (Li et al. 2023). Also, Nassr et al. introduced a link between the impact energy and the size of the damage on the sample (Nassr et al. 2021). Finally Angelides et al. discussed the time-temperature dependence of the interlayer yield stress (Angelides et al. 2021) and its influence on the post-fractured laminated glass bending behavior (Angelides et al. 2022). A large number of numerical models has been proposed to reproduce the crack pattern and to simulate the impact resistance of the laminated glass regarding the previous experimental results: using Rankine criterion for glass breakage (Pyttel et al. 2011; Alter et al. 2017; Fernandes et al. 2021), combined with cracking and element deletion (Hála et al. 2023), or a cohesive zone model between the layers (Chen et al. 2016; Shahriari and Saeidi Googarchin 2020). Peridynamic solution is also used to describe the crack pattern (Lai et al. 2018), the PVB/glass adhesion strength (Samieian et al. 2019), and the glass cracking plus interfacial debonding (Ma et al. 2022). The simulations generally give plausible results that are compared to post-fractured analyses of the laminated glass damage. However, it is more difficult to verify the consistency of the model at different times of a test because in-situ measurements on laminated glass under impact are very challenging, notably due to the structure change when cracks develop. Indeed, the relative movement of the fragments during the tests is seldom studied, the randomness and very

fine fragmentation requiring accurate measurement in time and space. This leads only to post-impact analyses of fragmented samples after rigid-body blunt impacts on laminates in the literature. These above-mentioned experimental works (Yu et al. 2017; Li et al. 2019; 2023; Nassr et al. 2021) have brought significant characteristics of the dynamic behavior of laminated glass through a few key quantities (*e.g.,* acceleration of the projectile, strain gauge measurement on the sample, high-speed mono-vision). Yet, these – mainly local – measurements do not provide a global quantitative picture of the whole plate, rendering the comparisons with the numerical modeling difficult and non-exhaustive.

The low-velocity rigid body impact on burglar-proof laminated glass as described in standard *EN 356* (European Norm 2000), corresponds to a series of three successive 4 kg steel ball drops from a height in the range of 1.5 m to 9 m, on a 1 m^2 laminate. This standard aims to prevent perforation, which is also important for protecting people against falls. To better apprehend this test, Nourry (Nourry 2005) designed an impact-test device, named *cannon*, that can operate on smaller laminated glass samples in a controlled and quantified way.

In a general context, the experimental tools to characterize the impact response of either impactor or laminated glass can be classified into three major categories:

1. Direct measurements on the projectile/impactor (Yu et al. 2017; Li et al. 2019; Wang et al. 2020; Li et al. 2023).
2. Detection of wave propagation on the glass surface via multiple strain gauges or accelerometers glued at different radial distances from the

impact location (Wang et al. 2020; Nassr et al. 2021).

3. Kinematic field measurements, combined with high-speed cameras capturing the *in-plane* cracking of the glass plies (Del Linz et al. 2017; Mohagheghian et al. 2017; Wang et al. 2021).

Compared to these other techniques, *Stereo-Digital Image Correlation* (Sutton et al. 2009) (S-DIC) is a non-contact, non-destructive, robust, and precise optical method to access 3D shape and kinematic information (motion and deformation) of large structures (Dufour et al. 2015b; Genovese and Sorgente 2018). For instance, the S-DIC is used to analyze blast loading experiments (Hooper et al. 2012) or bird strike experiments (Mohagheghian et al. 2018) and validate associated numerical models by comparing the deformed shape of the observed surface to the simulated one. Moreover, by expressing S-DIC into a global Finite Element based formulation, the virtual model (*e.g.,* CAD (Dufour et al. 2015a) or Finite Element mesh (Pierré et al. 2017; Berny 2020; Colantonio et al. 2020)) can be flexibly deformed to fit seamlessly with the real deformed 3D shape. This allows for shape characterization and kinematic field measurement of complex 3D objects, even for large deformation configurations.

The focus of the current study is mainly experimental via analyzing a *cannon* test. It is proposed to measure the glass shards formation and kinematics. Direct kinematic measurements on the sample will be compared to the kinematics of the impactor. The experimental set-up and the developed axisymmetric S-DIC code will be presented. The novelty of this paper lies in the use of a DIC regularization method exploiting the axisymmetry of the test to counter the numerous and severe artifacts that can occur during

the test, such as the change in brightness and contrast or the discontinuities (*i.e.,* cracks) on the measured surface.

The paper is organized as follows: section 2 introduces the *cannon* device and its stereo camera setup. Section 3 addresses the details of spatial-regularization implementation into an already existing global S-DIC code. The obtained results are presented and discussed in section 4. The first 3 ms of an impact are analyzed, including kinematic fields and crack pattern measurements, and the regularization is further discussed. Finally, section 5 draws some conclusions addressing, in particular, the consequences of the experimental observations for a numerical model of laminated glass dynamic behavior.

2. Experimental device and material

2.1. Experimental device

Initially developed by E. Nourry (Nourry 2005), the *cannon* test device aims at reproducing hard impacts (especially blunt and rigid objects) on laminated glass in a controlled way via a low-velocity/large-mass impact. The set-up allows the impact experiments to replicate the desired conditions by controlling the impactor velocity and the laminated glass sample characteristics (*e.g.,* layers thickness, previous damage). This concept was further explored through later studies, *e.g.,* Decourcelle's (Decourcelle 2011), and results were analyzed using tensile tests on pre-cracked laminated glass samples as a model describing impactor kinetic energy dissipation via delamination and tearing of the polymer ply (Elzière 2016). A key feature of this set-up is that it offers the measurement of the impactor head motion via a laser

telemeter at the high rate of 30 kHz, from which velocity (using finite difference) and kinetic energy can be estimated assuming the impactor head to be rigid (non-deformable).

This device allows testing different specimen thicknesses of the plies and materials to compare quantitatively their impact performances, with a good reproducibility and explore a range of impact velocity from 2 to 15 m/s.

The impacted samples are square-shaped plates of 300×300 mm^2: this surface is about 10 times smaller than that of ball-drop tests but corresponds to the size of the damaged surface during standard *EN 356* impacts. During the few tens of milliseconds of an impact experiment the boundary conditions — namely the fastening of the plate, the impactor geometry, and the center-to-edge distance — of the laminated glass plate drives the cracking of the glass and, hence, the PVB stretching and tearing. Here, the fastening of the glass is well-controlled and reproducible: two polished steel rings, with curvature radius of 1 mm in contact with the glass — large enough to avoid any sharp indentation —, and tightened by 4 screws at 10 N·m. Additionally, Decourcelle (Decourcelle 2011) highlighted mechanical wave propagation on the glass sample, provoking the first orthoradial cracks, are not significantly dependent on the sample size (Decourcelle 2011), justifying the use of smaller samples (*i.e.,* 300×300 mm^2) than in the norm *EN 356* (*i.e.,* 1100×900 mm^2). However it has an influence on more advanced stages of the test, where the finite strain regime and large out-of-plane bending is at stake.

As schematized in Fig 1, a projectile is set in motion via a compressed air shot, and hits the cylindrical end of the impactor. The impactor is composed of a cylindrical body, guided in a lubricated bronze barrel, whose head is a

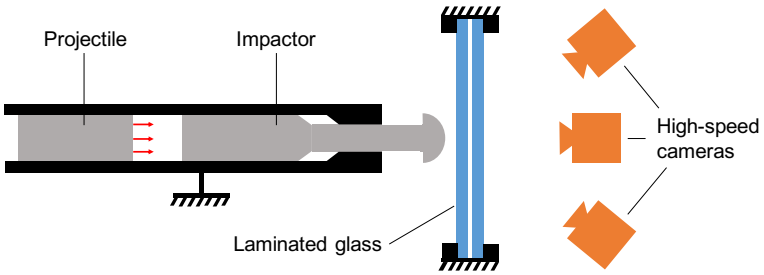

Fig 1: Scheme of a *cannon* experiment. The impactor and projectile are guided in the barrel. The impactor head finally hits the laminated glass with a normal impact. If the laminated glass is completely pierced, the impactor is stopped by an arrest cone in the barrel.

blunt half-sphere made of steel to replicate the contact surface of the ball-drop tests. The whole impactor weight is designed to be 4.3 kg. A telemeter measures via laser triangulation method, the hemisphere displacement at 30,000 Hz, with a 3 µm uncertainty. These high rate measurements allow to evaluate axial accelerations and velocities through finite difference. The impactor initial speed is $v_0 = 8.28$ m/s in the reported experiment. It is a median value of the impact velocity range reached on the device, that is also close to the P2A classification of the norm *EN 356*. In accordance with the laminate design, in the present case, the velocity is set to avoid perforation at the end of the impact.

During a typical fragmentation test with the *cannon*, the half-sphere apex impacts the glass surface at that initial velocity v_0 and with a normal incidence. In the first microseconds after impact, the laminate behaves elastically for the most part, while a small zone of the first ply right under the impactor head is crushed under intense multiaxial loading. Depending on the impact velocity and the sample strength, the first radial cracks may appear from the

plate center within a few microseconds to a few hundreds of microseconds. As the plate bends, the radial cracks extend and sometimes become denser, while orthoradial cracks are also formed. More and more cracks are created during the whole impact duration. When the fragmentation is well-advanced, the stretching (and possibly tearing out) of the PVB interlayer dissipates a large amount of the impact energy as the impactor stroke increases. This dissipation occurs at the PVB bridge locations that connect all the glass fragments (Seshadri et al. 2002).

The interlayer thickness can influence the time to tearing as a competition between delamination and stretching occurs: for high strain rates, less time is given for delamination initiation leading to a very large deformation of the interlayer that ends up tearing prematurely. Therefore, a thicker interlayer may sustain higher impact regimes as the delamination is given more time to initiate (Morison 2007; Hooper 2011; Angelides et al. 2019). In the present experiment, the laminated glass sample is composed of two 4 mm thick Planiclear® soda-lime glass plies, and a 0.76 mm PVB interlayer Saflex® RB41. The laminates are assembled in a clean room, degassed using an oven and a calender adhesion fully develops in a last stage where the laminate is placed in an autoclave, where the temperature is set to about 130°C and pressure to 13 bars for several hours.

2.2. Stereovision setup

Cameras, shown on Fig 2, are used to record the details of the dynamic fracture. The first camera (2) is a Shimadzu® 'HPV-X2' that captures the crack initiation at 100,000 Hz with a 400×250 pixel definition. The camera axis is coincident with the *cannon* z-axis. Two synchronized (at ±20 µs)

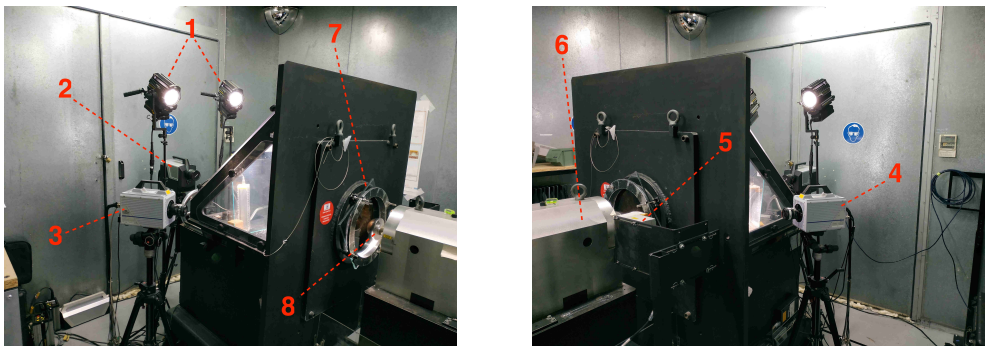

(a) (b)

Fig 2: The stereo camera setup: **1** The 400W spotlights. **2** Shimadzu® HPV-X2. **3** Right-view Photron® SA-5 (24 mm lens). **4** Left-view Photron® SA-5 (24 mm lens). **5** Telemeter. **6** Barrel box. **7** Laminated glass sample clamped in a circular window. **8** Impactor half-sphere.

Photron® 'SA-5' cameras (3 & 4) are positioned on each side of the device, monitored at 30,000 Hz. All images are 8-bit encoded (*i.e.,* the gray level of each pixel may vary from 0 to 255). The definition of the two lateral cameras decreases as the acquisition rate increases. In this experiment setting, their total definition is 640×376 pixels. Moreover, due to the very short exposure time ($\leq$ 30 µs) of the fast cameras, two 400 W spotlights are oriented towards the sample to provide enough light with negligible PVB heating. Indeed, due to the short exposure time it is not expected that temperature effects will influence the material properties of the interlayer.

The incident angle between the camera axes and the *cannon* principal axis varies on each side from 30° to 45° depending on the remaining space around the large test bench. All cameras are triggered using the same photo-electric sensor that detects the projectile presence a few milliseconds before its contact with the impactor, with a 40 kHz sampling rate.

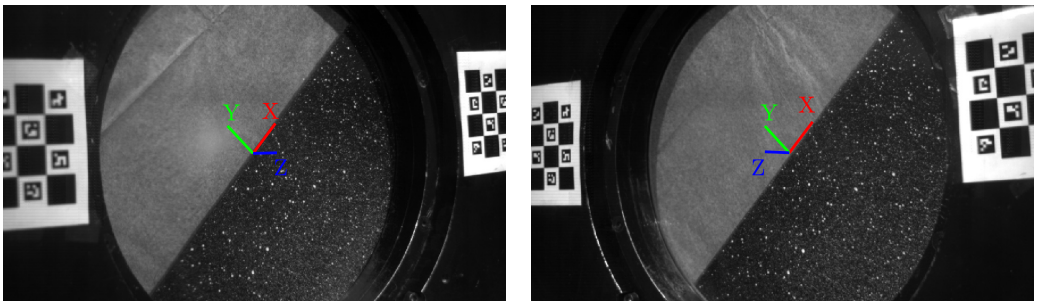

(a) Left side camera.

(b) Right side camera.

Fig 3: Initial view of the two lateral cameras. World coordinate system projected on the images, validating the calibration of the presented stereoscopic camera system.

Observing the back surface of the laminated glass at high temporal resolution has two motivations: first, the measurement of surface deformation, and second, the characterization of glass plies fragmentation. Unfortunately, these two goals are mutually exclusive. Indeed, the kinematics of the back surface can be obtained from S-DIC, provided a surface marking with a speckle pattern is deposited on the back face. In turn, the formation of cracks is mostly hidden due to the opaque paint presence. To circumvent these difficulties, a black and white speckle pattern is applied on the back surface of the laminated glass sample, covering the right-bottom part of the laminated glass, providing sufficient Gray Level (GL) contrast to perform S-DIC measurements (Fig 3). The left-top part is left transparent, but a thin tissue paper is interleaved between the projectile and the sample, to observe the formation of crack patterns on a uniform background (masking the background scene that makes cracks more difficult to read). The interest of painting only one half of the plate is to allow for an easy association between the evolving cracking pattern of the laminated glass and the deformed surface

measured via S-DIC. Having access to these cracks evolution gives information on the time duration of the elastic deformation phase of the sample, the formation of the radial cracks, orthoradial ones, the beginning of the tearing phase and the perforation step for instance. The S-DIC measurements can also be extrapolated on the non-speckled area of the plate, and therefore a measurement of the cracks evolution via the residuals is made possible on the reference surface. Table 1 summarizes all the extrinsic DIC parameters.

Cameras	Photron® SA-5
Definition	640×376 pixels
Gray Levels rendering	8 bits
Lens	Nikon AF Nikkor 24mm f/2.8D
Aperture	f/11
Field of view	500 mm $\times$ 300 mm
Image scale	≈ 0.7 mm/px (in the center)
Stereo-angle	right camera: 33°, left camera: 37°
Stand-off distance	between 70 and 80 cm
Image acquisition rate	30,000 Hz
Patterning technique	white dots over black surface
Pattern feature size	in the range of 3 to 10 pixels

Table 1: DIC hardware parameters

A trustworthy calibration of stereo-camera system is essential to perform a 3D kinematic measurement during the dynamic testing. Therefore the calibration procedure is further explained in Appendix A.

3. Axisymmetric S-DIC analysis

Stereo-Digital Image Correlation (S-DIC) constitutes a technique of choice to measure, on the one hand, the plate global and time resolved deformation and, on the other hand, the crack pattern evolution, which leads to the estimation of PVB stretching at the glass plies cracks.

In the experiment, the laminated glass deformation is monitored by the two lateral cameras. The out-of-plane displacement field is obtained from a S-DIC analysis (using Correli 3.0 software (Leclerc et al. 2015)) during the first 3 ms (*i.e.,* 90 images) of the experiment. During this period of time, global S-DIC can be performed over the speckle surface: the elastomeric paint remains elastic and only a few radial cracks can be observed on the DIC residuals. A change in brightness takes place on the deformed surface because of light reflection as the impactor penetrates into the laminate.

3.1. Global S-DIC procedure

The global S-DIC procedure and the used notations are shortly recalled thereafter and detailed in Appendix B and interested readers can refer to previous publications (Hild and Roux 2012; Dufour et al. 2015b; Berny 2020) for a more extended presentation.

The specimen kinematics is described in 3D by a displacement field $\mathbf{U}(\mathbf{X})$ such that a material point $\mathbf{X}$ in the reference configuration moves to a new position $\mathbf{X}' = \mathbf{X} + \mathbf{U}(\mathbf{X})$. For each camera, labeled c, the projective model allows relating the 3D point to its position in the camera image plane, $s\mathbf{x}^c = [\mathbf{\Pi}]^c\mathbf{X}$, and hence its movement obeys $s\mathbf{x}'^c = s\left(\mathbf{x}^c + \mathbf{u}^c\right) = [\mathbf{\Pi}]^c(\mathbf{X} + \mathbf{U}(\mathbf{X}))$. Grey level conservation between the reference image f^c (captured by camera

c) and the deformed one g^c (from the same camera) is a basic assumption of Digital Image Correlation that leads to the determination of the kinematic as the minimization of the L2 norm of the so-called residual field

$$\varrho^c(\mathbf{X}, \mathbf{U}(\mathbf{X})) = \left[g^c(\mathbf{x'}^c) - f^c(\mathbf{x}^c)\right] \tag{1}$$

This minimization is performed based on a parametrization of the kinematics $\mathbf{U}$, chosen here as supported by a 3D finite element mesh, namely $\mathbf{U}(\mathbf{X}) = \sum_i U_i \theta_i(\mathbf{X})$ where θ_i is the shape function vector associated to node i, and U_i the nodal amplitude. These nodal displacements gathered into a vector $\{\mathbf{U}\}$ are computed using a Gauss-Newton algorithm, namely progressively correcting the displacement with a correction vector $\{\delta\mathbf{U}\}$, solution of the tangent problem

$$\sum_{c=1}^{N_c} [\mathbf{H}]^c \cdot \{\delta\mathbf{U}\} = \sum_{c=1}^{N_c} \{\mathbf{b}\}^c \tag{2}$$

where the Hessian $[\mathbf{H}]^c$ and second member $\{\mathbf{b}\}^c$ are sums over all cameras c of individual contributions

$$\begin{aligned} H_{ij}^c &= \sum_{\mathbf{X}\in \mathrm{ROI}} \left[\frac{\partial \mathbf{u}^c}{\partial U_i} \cdot \nabla f^c(\mathbf{x}^c)\right] \left[\frac{\partial \mathbf{u}^c}{\partial U_j} \cdot \nabla f^c(\mathbf{x}^c)\right] \\ b_i^c &= \sum_{\mathbf{X}\in \mathrm{ROI}} \left[\frac{\partial \mathbf{u}^c}{\partial U_i} \cdot \nabla f^c(\mathbf{x}^c)\right] \left[f^c(\mathbf{x}^c) - g^c(\mathbf{x'}^c)\right] \end{aligned} \tag{3}$$

The S-DIC problem is intrinsically an ill-conditioned (if not ill-posed) problem. The use of Tikhonov regularization improves the numerical conditioning of the problem, but at the expense of diverting the solution from reality because it is a numerical 'trick' whose physical justification is ill-founded. As a consequence, it may lead to artifacts when for instance large rotations occur (Colantonio et al. 2020). The ideal solution would be to help

the problem formulation using a mechanical modeling of the laminated glass response. However, the fragmentation of the glass plies, the delamination of the PVB and its extension involving significant geometric non-linearities (large displacements and rotations) makes this route quite challenging. Alternatively, the axisymmetry of the set-up is a very strong constraint which may be used for regularization without any prior knowledge or fragile assumption about the mechanical model of the monitored sample, even if this symmetry is expected to be broken locally in the long run as the laminated glass is fragmented, and finally torn apart. For global S-DIC, the T3-mesh pre-

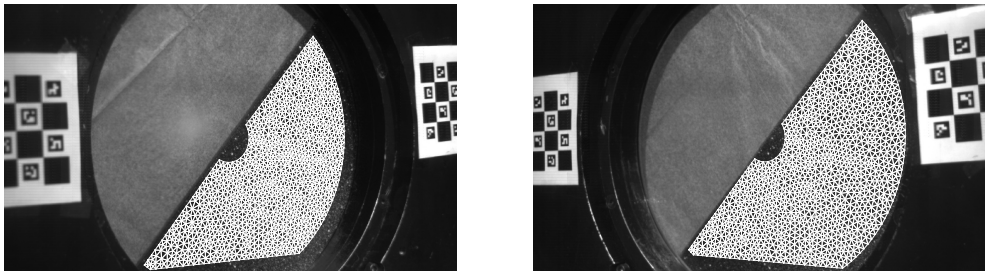

(a) Mesh on left side camera.

(b) Mesh on right side camera.

Fig 4: Initial 2D mesh projected on the 2 reference frames. All are T3 elements of 4 mm average length.

sented 4 mm length elements that are superimposed on the reference frames on Fig 4. There is a total of 2366 elements and each element possesses 32 integration points, so that all gray level information on the images is considered during S-DIC calculation. S-DIC parameters are mentioned in table 2.

DIC software	Correli 3.0 (Leclerc et al. 2015)
Element sizes	4 mm ($\approx$ 12 px)
Number of elements	2366
Shape functions	Linear (T3 elements)
Evaluation points (per element)	32
Displacement noise-floor	$\leq$ 40 µm

Table 2: Global S-DIC parameters

3.2. Axisymmetric S-DIC

A new global axisymmetric description of the displacement field can be inserted as a constraint for the minimization problem. The axisymmetric based regularization proposed thereafter is a non-invasive constraint that resumes the unknown displacement field (3D vector field over a 2D surface) to a much simpler one (2D displacement field over a 1D radial profile). Such a regularization could be done with B-splines for instance (Chapelier et al. 2021), but a piece-wise linear description will be adopted in the following. It can be seen as a reduction of the degrees of freedom of the initial mesh nodal displacements.

Expressed in cylindrical coordinates, the displacement between two images is a purely radial and out-of-plane displacement

$$\mathbf{U^{ax}}(r) = [\mathbf{U}_r(r),\ 0,\ \mathbf{U}_Z(r)]$$

The radius being directly $r_i = \sqrt{X_i^2 + Y_i^2}$ and the angle $\alpha_i = \arctan(Y_i/X_i)$.

The orthoradial displacement is enforced to be globally null, which remains a reasonable assumption as long as no tear opens up in the interlayer

(a phenomenon, local at first, that propagates and breaks the axisymmetry of the deformation even at a global scale). Radial and axial displacements only depend on the radial distance r between the impact location and the nodal position. The FE mesh center is localized at the impact initial position, *i.e.*, the center of the laminated glass plate, with a 200 µm uncertainty.

The transformation from cartesian to cylindrical coordinates is written as a rotation matrix $[\mathbf{P}]$, combining the smaller transfer matrices $\mathbf{P}_i$ for each node i

$$\mathbf{P}_i = \begin{bmatrix} \cos\alpha_i & -\sin\alpha_i & 0 \\ \sin\alpha_i & \cos\alpha_i & 0 \\ 0 & 0 & 1 \end{bmatrix} \tag{4}$$

such as

$$\mathbf{U}(\mathbf{X}_i) = \mathbf{P}_i \mathbf{U}^{\mathbf{ax}}(r_i) \tag{5}$$

The axisymmetric description will be enforced via the introduction of 1D-linear shape functions (Fig 5), limiting the displacement measurement along r and Z directions. The 2D-mesh current nodal position (represented by circles) are represented on the new shape functions.

In addition, rigid modes constraining all the nodes in respectively X, Y and Z directions, are added to possibly compensate the experimental Z-axis location error during the axisymmetric S-DIC procedure. In other words, the addition of those three additional modes allows to shift and correct the symmetry axis location.

The 1D shape functions are noted $q_i(r)$ and filled in a second transfer

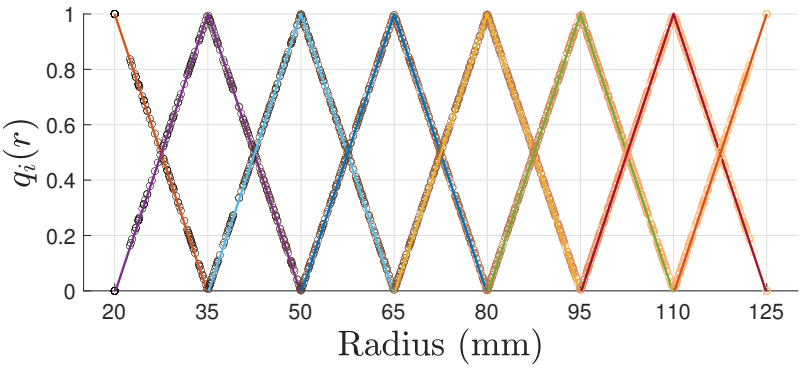

Fig 5: 1D shape functions $q_i(r)$ insuring displacement continuity, in straight lines. Interpolated T3-nodes (Fig 4), as circles on the new shape functions. For better readability the plot illustrates 15 mm-long elements, while 4 mm elements were actually used in the DIC measurements.

346 matrix $[\mathbf{Q}]$ such as the new Hessian and right-hand terms become

$$\begin{aligned} [\mathbf{H}]^{ax} &= ([\mathbf{P}][\mathbf{Q}])^{\top} \cdot \left(\sum_{c=1}^{N_c} [\mathbf{H}]^c \right) \cdot [\mathbf{P}][\mathbf{Q}] \\ \{\mathbf{b}\}^{ax} &= ([\mathbf{P}][\mathbf{Q}])^{\top} \cdot \left(\sum_{c=1}^{N_c} \{\mathbf{b}\}^c \right) \end{aligned} \tag{6}$$

347 and the minimization problem

$$[\mathbf{H}]^{ax} \cdot \{\delta \mathbf{U}\}^{ax} = \{\mathbf{b}\}^{ax} \tag{7}$$

348 The global 3D-displacement increment $\{\delta \mathbf{U}\}$ is updated via the two transfer
349 matrices and the nodal axisymmetric displacement $\{\delta \mathbf{U}\}^{ax}$

$$\{\delta \mathbf{U}\} = [\mathbf{P}][\mathbf{Q}] \cdot \{\delta \mathbf{U}\}^{ax} \tag{8}$$

350 This newly introduced reduced problem is far better conditioned than the
351 original S-DIC one (decreasing the degrees of freedom from 7098 to 84).

Therefore no additional regularization is needed to perform axisymmetric S-DIC.

4. Results and discussion

Global S-DIC and axisymmetric S-DIC have been performed on the painted deformed surface of the laminated glass, during the first 3 milliseconds following impact, or a total of 90 frames per camera. Results at different times are shown in figures 6, 7 and 8, corresponding respectively to the 20^{th}, 50^{th} and 80^{th} frames. Both raw camera images, (a) left view and (b) right view, are represented in gray levels. Then the left column corresponds to the global S-DIC analysis and the right column to the axisymmetric S-DIC analysis, with: (c)+(d) the measured residuals by the left-side camera (image (a)), (e)+(f) the measured residuals by the right-side camera (image (b)), (g)+(h) the out-of-plane displacement field on the reference mesh and (i)+(j) the current deformed 3D surface.

A crushed glass zone, centered at the impact point appears as a bright white zone in Fig 6a-b. The formation of radial and orthoradial cracks could be observed during the whole experiment. First, radial cracks propagate from the impact point to the edge, so that fragment sizes increase with the distance from the center. Then orthoradial cracks appear, as can already be seen in Fig 6a-b. As time passes, the density of both radial and orthoradial cracks increases, leading to smaller and smaller fragments.

This growing crack number also increases the deformability of the fragmented laminated glass plate, whose glass shards are still connected by interlayer polymeric bridges that sustain large strains.

The geometry of the deformed plate surface could at first be approximated by a rounded cone of increasing height. This information could also be read on the displacement fields (g-j) for the three figures 6, 7 and 8.

The sample shape evolution and fragment orientation induce some light reflection, with severe gray level changes on the captured images. Specular reflections are even observed in some images, (such as the white spot at the top of Fig 8a), making the analysis more and more difficult for the S-DIC software.

A brightness change, not being accounted for by the S-DIC procedure, is finally present in the residual field Fig 6(c-f). In particular, a contrast in the residual field across a radial boundary, may be interpreted as a localized bending along a radial crack, making some of them apparent although they could hardly be perceived in the raw images.

In addition, due to the change in brightness in the right-hand zone, very large (erroneous) displacements are obtained at some isolated nodes (see Fig 8i) because of the extreme violation of the gray level conservation assumption. This kind of displacement is however well filtered with the axisymmetric regularized displacement (Fig 8j).

In Fig 7(c-f) and even more in Fig 8(c-f) axisymmetric regularization gives rise to a larger rms residual, and yet the displacements are very precisely equal to the trustful part of the non-regularized S-DIC computation. Indeed, each local non-axisymmetric displacement is correctly accounted for in the axisymmetric regularized version, without altering the measurement.

The cracks are easier to identify on the residual fields (c-f) for advanced steps of the test as stretching and delamination of the PVB bridges increase.

The separation between two fragments split by a crack may reach about one millimeter, and becomes very clearly visible on the DIC residuals as the pixel size is approximately 1 mm.

Accessing the final crack pattern by an examination of the post-fractured sample in fragmentation experiment is not easy as many non-reversible phenomena occur: large stretching then tearing of the interlayer, delamination between the PVB and the glass shards, comminution at the center of the plate that loses smaller fragments sometimes crushed into glass dust. Therefore the glass damage is hard to qualify, evolving throughout the whole test duration. Three pictures have been taken at the end of this experiment (Fig 9). As can be seen, the PVB layer has been torn and glass fragments are missing close to the impact location. Farther along the radial direction, the laminated glass retains a crater-like or cone-like shape at the end of the experiment which emphasizes a residual irreversible deformation of the plate. The failure mode encountered during this test can be assimilated to punching failure (Li et al. 2023) as the area under the impactor is very finely fragmented and the tearing occurred at 40 mm – very close – to the center of the plate where glass fragments detached from the adhesive layer. Large fragments areas, located at more than 100 mm from the impact, may still sustain secondary impacts as the local delamination and PVB stretching has been very low.

Many cracks can be observed on these three images, thanks to a good spatial resolution, but the temporal damage qualification cannot be assessed via post-fractured imaging. In the following is proposed a live monitoring of the crack formation to complete the damage analysis.

Due to the global axisymmetry of the measured displacement field, it is

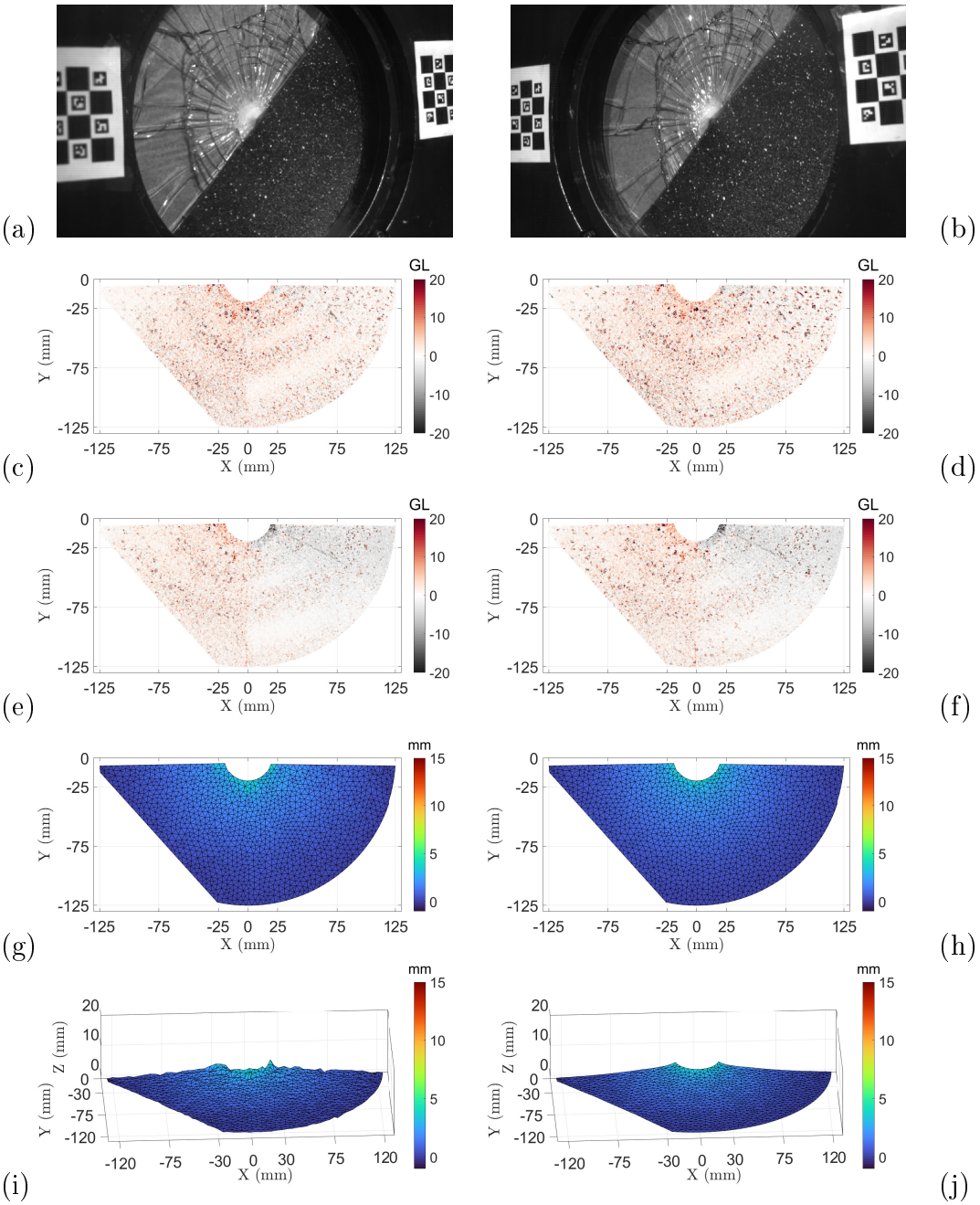

Fig 6: S-DIC measurement at t=0.63 ms (*i.e.*, iteration 20): (a)+(b) Stereo images. Corresponding residual fields at convergence (in gray levels): (c)+(e) S-DIC (d)+(f) Axisymmetric. The out-of-plane displacement field on initial mesh (mm): (g) S-DIC (h) Axisymmetric. Idem on deformed mesh (mm): (i) S-DIC (j) Axisymmetric.

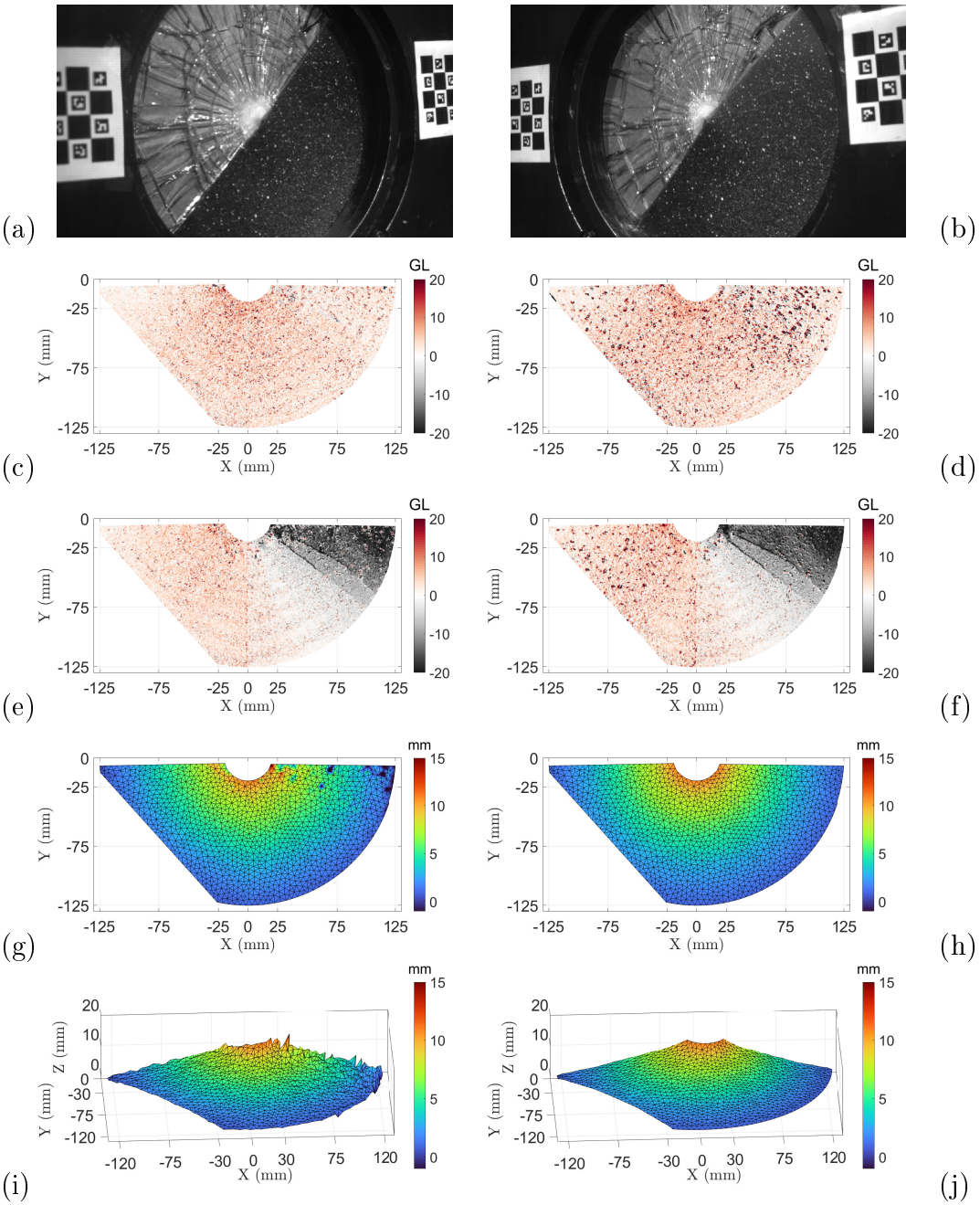

Fig 7: S-DIC measurement at t=1.63 ms (*i.e.*, iteration 50): (a)+(b) Stereo images. Corresponding residual fields at convergence (in gray levels): (c)+(e) S-DIC (d)+(f) Axisymmetric. The out-of-plane displacement field on initial mesh (mm): (g) S-DIC (h) Axisymmetric. Idem on deformed mesh (mm): (i) S-DIC (j) Axisymmetric.

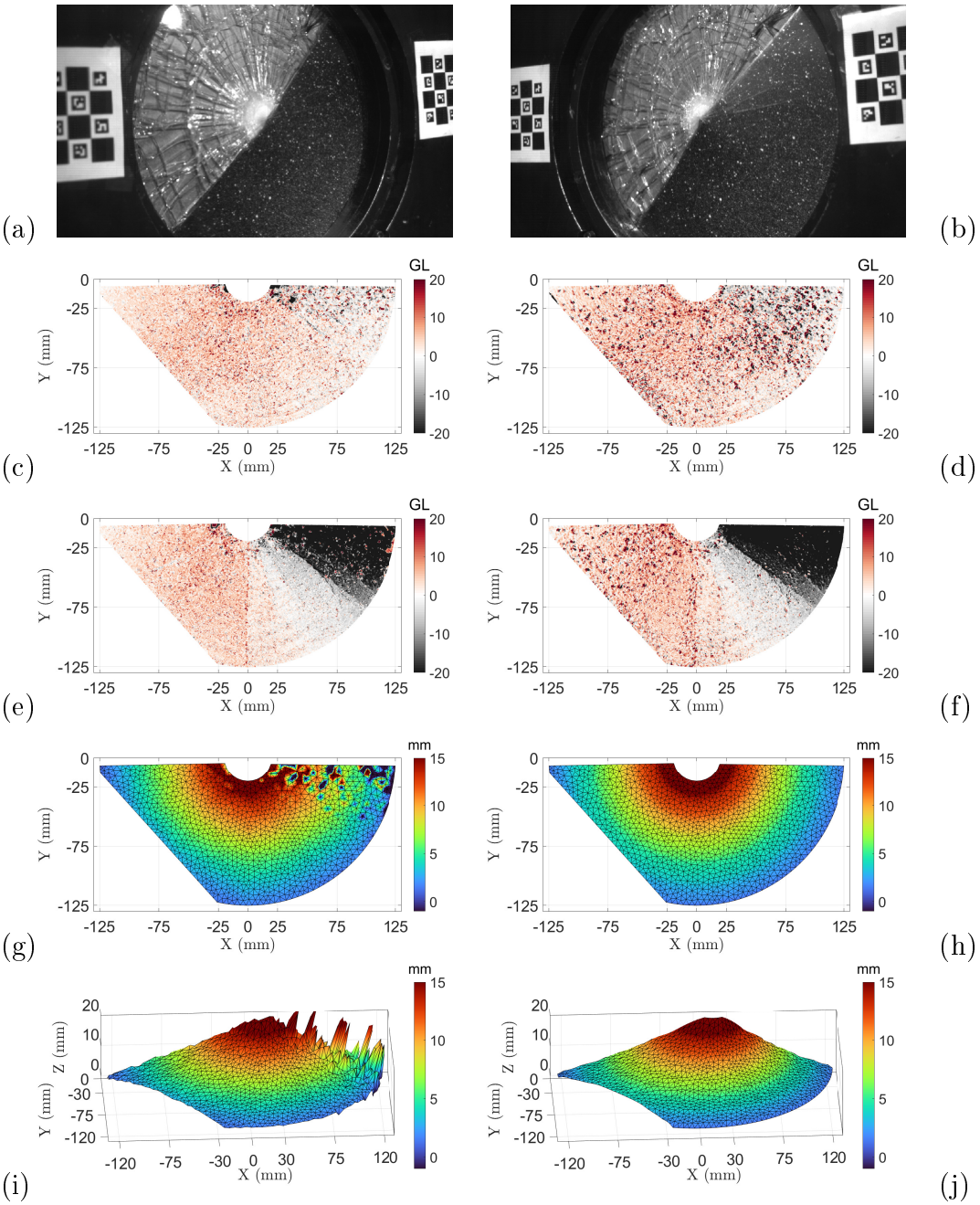

Fig 8: S-DIC measurement at t=2.63 ms (*i.e.*, iteration 80): (a)+(b) Stereo images. Corresponding residual fields at convergence (in gray levels): (c)+(e) S-DIC (d)+(f) Axisymmetric. The out-of-plane displacement field on initial mesh (mm): (g) S-DIC (h) Axisymmetric. Idem on deformed mesh (mm): (i) S-DIC (j) Axisymmetric.

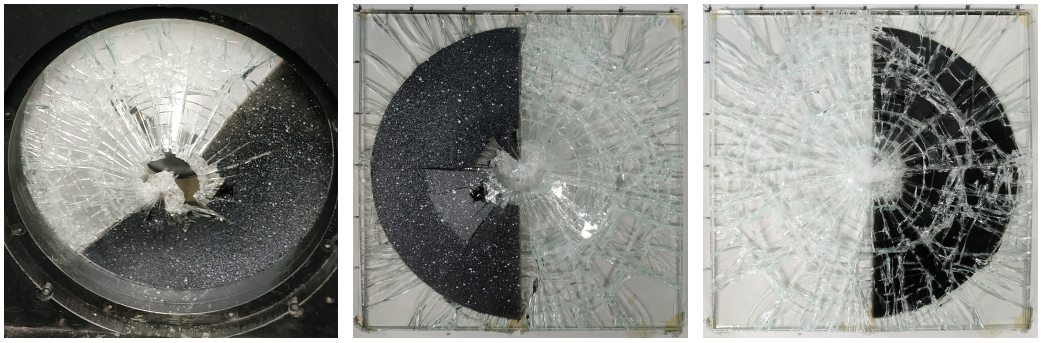

(a) Post-impact sample (b) Back side view (c) Impacted side view

Fig 9: Post-breakage sample observations performed just after the experiment: (a) sample is still set in the device. Flat positions: (b) Back side or monitored side view, (c) Front side or impacted side view.

possible to estimate the deformation of the non-speckled glass surface on a semi circular mesh, then analyze the residuals between a reference non fragmented image and the experimental deformed image in the Lagrangian frame. Some residuals of the non-speckled part are represented on Fig 10. The highest gray level value residuals correspond to cracks location in the glass plies. It is possible to follow their length throughout the experiment. First, on Fig 10a-b, radial cracks are growing from the impact location toward the sample edges. Intense radial stresses initiate a few first orthoradial (circular) cracks, for example in Fig 10a, at coordinates (25, 75) and (-40, 50) millimeters. An area between 60 mm to 90 mm radius (Fig 10c-j), concentrates many orthoradial cracks, and delimits the finer fragmented area at the center of the plate from the larger fragmented zone at higher radius. This circular boundary was highlighted in Nourry's thesis and drives the global response of the laminated glass subjected to blunt impact (Nourry 2005).

Some limits can be mentioned in terms of crack measurement accuracy.

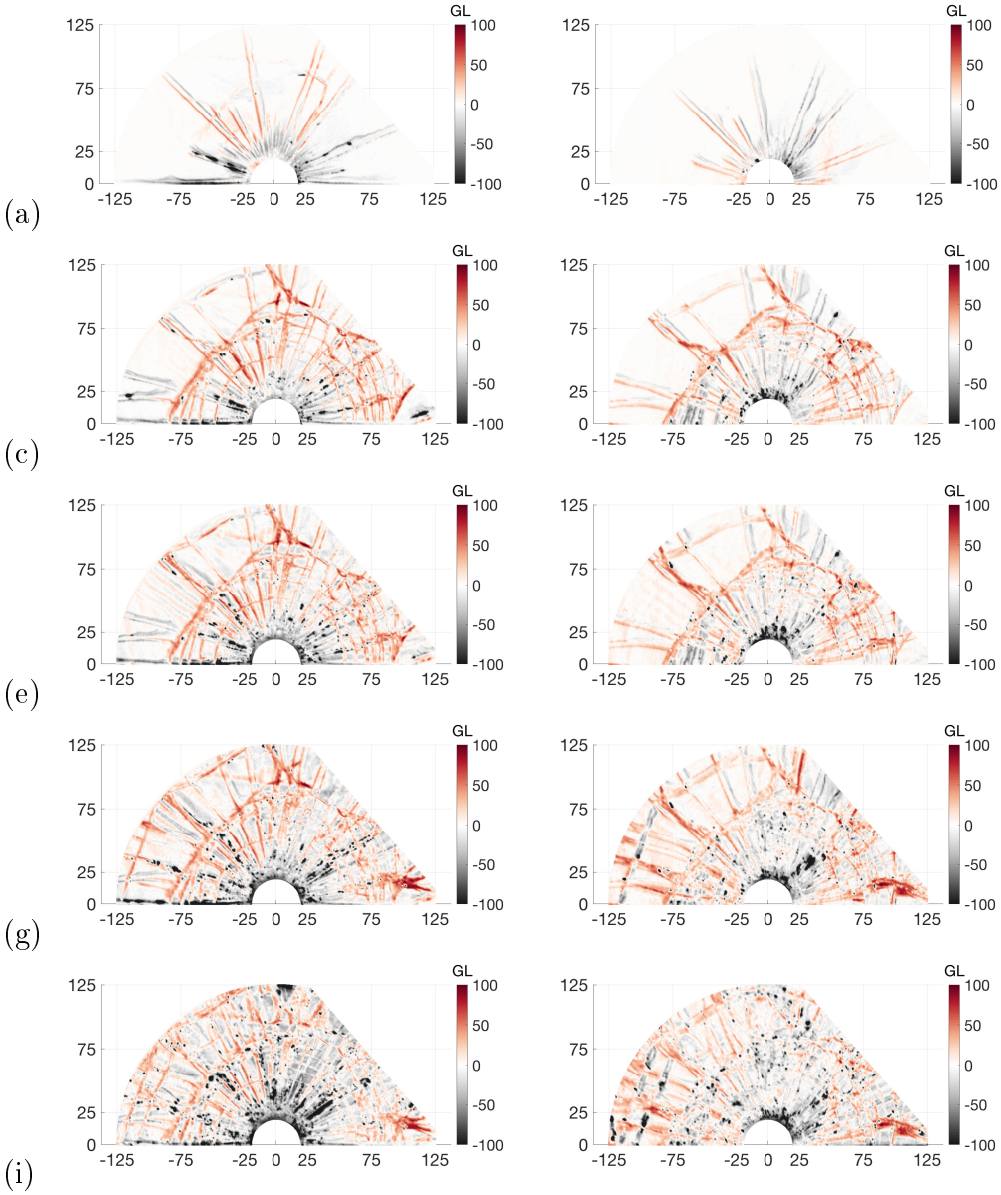

Fig 10: Residuals of the non-speckled area of the glass surface, projected on Z=0 mm plane. (a)-(b) t=0.40 ms. (c)-(d) t=0.63 ms. (e)-(f) t=1.13 ms. (g)-(h) t=1.63 ms. (i)-(j) t=2.63 ms. Left and right columns corresponds respectively to the left-side and right-side camera.

The first one is the crack duplication on the residual maps, caused by their projected shadows on tissue paper. This effect can be illustrated by the measured residual map of Fig 10c (same instant than Fig 6a) where cracks shadows can be seen. The effect might have been reduced using a darker tissue paper as a uniform background. A second limitation is due to the angular shift between the cameras and the device axis. This is enhanced by the large stretching of the PVB links between glass fragments, and by the widening cracks during the plate movement (see Fig 10j for instance). The stack thickness is also a limitation, as a radial crack can propagate in the first and second ply, and let a large imprint on the residuals. It can also be noted that the 20 µs temporal uncertainty in stereo-vision has to be adjusted to measure a synchronized crack formation, as a crack pattern difference is measured between Fig 10a and b.

A rapid increase of the S-DIC residuals is observed between frame 1 and 10 (Fig 11). Theses images correspond to the apparition of the radial cracks and the first orthoradial cracks. Then a slower growth of the residuals is observed up to frame 80. This evolution corresponds to the continuing formation of cracks on the plate and the increasing out-of-plane displacement. The larger contribution of the global residual ϱ is attributed to the change in brightness and contrast, but the increasing number of nodes being attributed an obviously incorrect displacement becomes dominant past image number 80. Therefore, from this point and on, the axisymmetric S-DIC global residuals grow more slowly and actually become smaller than the regular S-DIC ones.

The out-of-plane displacement field is globally well measured by S-DIC,

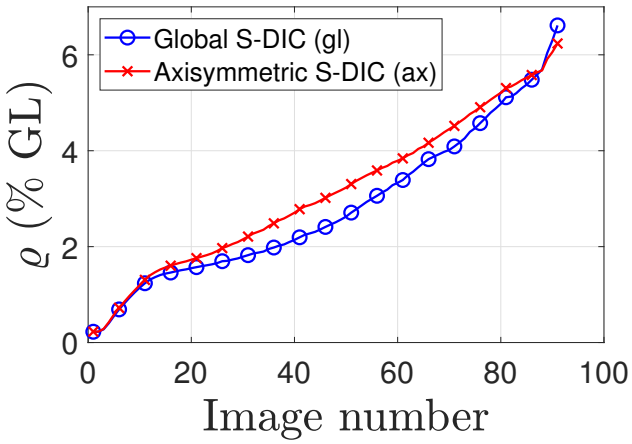

Fig 11: The global residual ϱ evolution is represented as a function of image number.

although some nodes do not converge properly on the displacement fields (g)+(i) of Fig 7 and 8. Those were located at a small distance from the center of the mesh and in the very intense brightness change zones. Those erroneous measurements are cleaned up in the axisymmetric S-DIC measurement (h)+(j).

Moreover, an axisymmetric interpretation of the displacement fields is represented on Fig 12, interpolating the S-DIC obtained fields on radial shape functions (legend '**gl**'). The out-of-plane displacement is therefore filtered, and a good radial approximation of the displacement can be obtained reducing the influence of the ill-behaved measurement points. The extrapolated displacement also matches the telemeter curve (black straight line), that can be interpreted as the displacement along the axis ($r = 0$), and fits the axisymmetric S-DIC results (legend '**ax**'). The telemeter is used to map the deformation of the crushed zone where S-DIC cannot measure the kinematic fields due to very large discontinuities (Meyland et al. 2023). For large radius

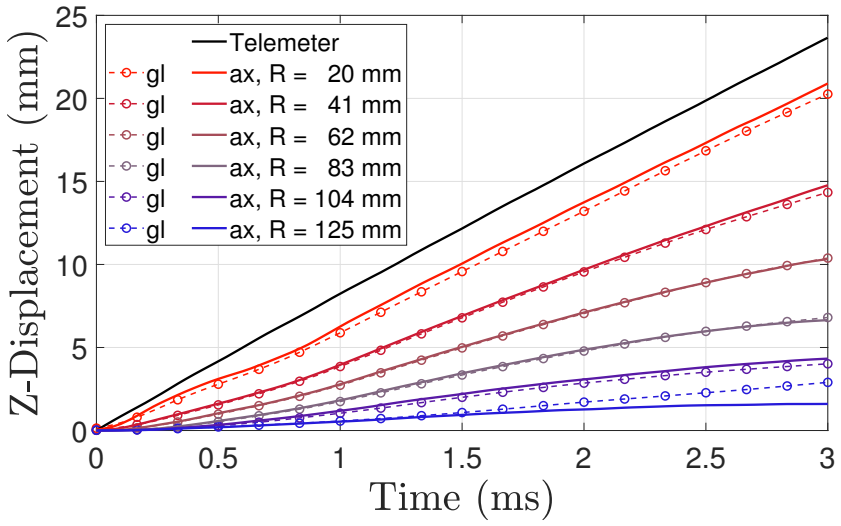

Fig 12: Out-of-plane displacement (mm) for some radius ('R', in mm) versus time (ms). Axisymmetric ('ax') and global ('gl') S-DIC are compared with the telemeter measurement.

and time, the global and axisymmetric results are moving away from each other showing that the axisymmetric code is more reliable than the initial global S-DIC procedure.

During the impact experiment, two areas can be distinguished: the first one right under the impactor head that which is finely fragmented, subjected to intense shear stress, quickly prone to tearing, and thus not able to dissipate a large amount of impact energy. The second area, starting from about 70 mm from the plate center, consists of glass fragments – connected via polymeric bridging – where the interlayer is still able to sustain large strains and delamination from the glass without introducing a significant bending of the glass plies and shearing of the interlayer. Thanks to the S-DIC measurements the strain rate was estimated to 5 to 10 s^{-1} that matches the order of magnitude of the membrane behavior – allowing delamination and stretching

– as introduced by Hooper (Hooper 2011). This membrane behavior is also validated by authors as the out-of-plane displacement exceeds the laminated glass thickness during the test (Angelides et al. 2019). The energy dissipation that occurs during an impact (such as the *cannon* experiment) through delamination and stretching of a polymer layer can therefore be estimated using the *through-crack tensile* (TCT) test, widely documented in the literature (Seshadri et al. 2002; Elzière 2016; Del Linz et al. 2017; Samieian et al. 2018; Fourton et al. 2020; Ma et al. 2022). This tensile test is performed on two pieces of laminated glass connected by a PVB ligament whose delamination front and stretching evolve. It has been pushed to cover a very large range of velocities from quasi-static regimes up to 10 m/s (Del Linz et al. 2017), matching the *cannon* velocity range. Therefore, the link between the interlayer stretching and its delamination from the glass shards is already well documented. Thanks to the kinematic field and the cracking pattern measurements presented in this article, it is possible to consider a model using the measured data with the TCT to describe the correct behavior of a fragmented laminated glass plate under a hard-body blunt impact during a *cannon* test. Those data are of interest to the experimenter to determine the behavior of different areas of the laminate, rather than relying only on either a local measurement via strain gauges or measurements on the impactor, that do not give the whole plate kinematics. Each laminated glass fragment has its own specific movement during an impact that can be interpreted as a local TCT test. In a nutshell, these measurements, coupled with a correct corresponding model of the fragmented laminated glass plate, should allow the evaluation of the local dissipated impact energy at the glass fragments

edges and, after summation over all cracks, the evaluation of the total energy absorbed by the broken laminated glass plate.

5. Conclusion

This paper studied a hard-body impact on a laminated glass using stereo-digital image correlation with high-speed cameras. During the fragmentation test, S-DIC analyses are carried out to extract the 3D shape variation and the corresponding kinematic information of the laminated glass.

The S-DIC algorithm demonstrates its versatility in obtaining 3D shape and field measurements. Using an FE-based mesh as a numerical model, it is possible to update and deform the virtual model to seamlessly fit the 3D shape variation, which allows the complex 3D kinematics to be resolved even in the late stage of the impactor stroke (as in the case of the presented fragmentation test on laminated glass). The newly developed axisymmetric description of the displacement field in S-DIC, which can be seen as a relevant geometric regularization devoid of other material-based mechanical assumptions, provides a remarkable robustness to the analysis, with very good convergence properties. The obtained performances are much greater with the help of this regularization which avoids the divergence of some nodes of the mesh and allows the crack formation to be measured on the deformed non-speckled part of the laminated glass.

In the context of laminated glass under impact monitoring fragmentation and large strain regime, S-DIC using a global formulation, is a powerful measurement technique, allowing access to the fragmented plate-deformed surface and crack density over the region of interest. However, many hy-

potheses were set to finally measure satisfying kinematic fields, countering the ill-posed DIC problem (that can add displacement error). The very extreme experimental conditions: ephemerous flashes of light, varying light intensity, cracks, and discontinuities formation, finite strain regimes. all contribute to make this test a very challenging one for S-DIC. Nevertheless, the proposed axisymmetric regularization allowed to overcome many of those obstacles.

From the present analysis, some directions of progress can be identified for future developments:

- Adding contrast and brightness correction should make the analysis more robust
- Considering the image series as a whole for a suited spatio-temporal analysis may further extend the domain of applicability of S-DIC
- Model reduction techniques, coupled to the latter spatio-temporal analysis may further accelerate the computations, and reduce the number of global kinematic unknowns.

Those directions are currently being investigated, and open promising perspectives.

The data treatment presented here gives access to the shape of the laminated glass during the impact, yielding the geometrical link between the energy dissipation close to the cracks (energy per delaminated area that can be measured on TCT experiments), the crack pattern evolution over the whole plate, and the global energy effectively dissipated (the diminution of kinetic energy lost by the impactor). This link will be exploited to build a

model that computes the energy that the laminated glass can absorb as a function of material parameters only, such as the glass-interlayer adherence or its large-deformation stress-strain behavior to be presented in a forthcoming publication.

Appendix A. Calibration of the Stereo Vision Camera System

Finding the correspondence between the 3D coordinates of known points in the specimen and their projected 2D coordinates in retinal images captured by stereo cameras (2 cameras or more) is crucial for accurate 3D shape reconstruction. This is performed in a so-called 'calibration stage', which consists in identifying the projection matrix (*i.e.,* $[\mathbf{\Pi}]$) to bridge the 3D coordinates of points, $(X, Y, Z, 1)^\top$ in the lab frame, to their 2D projection, $(x, y, 1)^\top$ in the camera image plane.

$$\begin{pmatrix} sx \\ sy \\ s \end{pmatrix} = [\mathbf{\Pi}]^j \begin{pmatrix} X \\ Y \\ Z \\ 1 \end{pmatrix} = [\mathbf{K}][\mathbf{RT}] \begin{pmatrix} X \\ Y \\ Z \\ 1 \end{pmatrix} \tag{A.1}$$

The projection matrix, $[\mathbf{\Pi}]$, can be decomposed into an intrinsic matrix, $[\mathbf{K}]$ — which characterizes the intrinsic parameters of camera (optical center, focal distance and skewness) — and an extrinsic projection matrix, $[\mathbf{RT}]$, which gives the relative position of the camera and 3D object (translation and rotation). s is a scale factor.

The projection matrix $[\mathbf{\Pi}]$ of each camera is commonly measured via a calibration object (Besnard 2010; Dufour et al. 2015b; Berny 2020). The technique consists in monitoring this well-known object, whose geometry and

size have been independently measured and stored for instance as a 3D-mesh file, expressed with the world coordinates of the problem. Both, intrinsic and extrinsic matrices, are identified thanks to the presented 'self-calibration' procedure.

A classical Point-to-Point initialization using natural features (*e.g.,* edge and corners), provides an initial guess of the projection matrix. Then, the projection matrices are further refined in the Global CAD/FE-based framework as proposed by (Dufour et al. 2015a; Shao et al. 2016; Berny 2020). Then comparing the gray level monitored by each camera at predefined integration points location, the second phase of calibration provides a refined determination of the projection matrices (Berny 2020; Beaubier et al. 2012).

In this study, the calibration target is a dihedral ("open-book") which has two square faces of 10 cm (±10 µm) side oriented at 130° (Besnard 2010) (see Fig A.13b-e). An external support is printed to position the object at the center of the circular window. The 3D printer accuracy is estimated at 200 µm.

An FE mesh (Fig A.13a) is used throughout this paper as the virtual model of the calibration target, where $n = 1, ..., N$ key points are selected in both the image (Fig A.13b-c) and virtual model (Fig A.13a) denoted as $\mathbf{x}_n$ and $\mathbf{X}_n$ respectively. The initialization of projection matrix, consists in minimizing the sum of quadratic differences

$$\mathcal{T} = \sum_{n=1}^{N} (\mathbf{x}_n - [\mathbf{\Pi}]\mathbf{X}_n)^2 \tag{A.2}$$

with respect to $\mathbf{\Pi}$. Initialization is validated by projecting the 3D mesh over

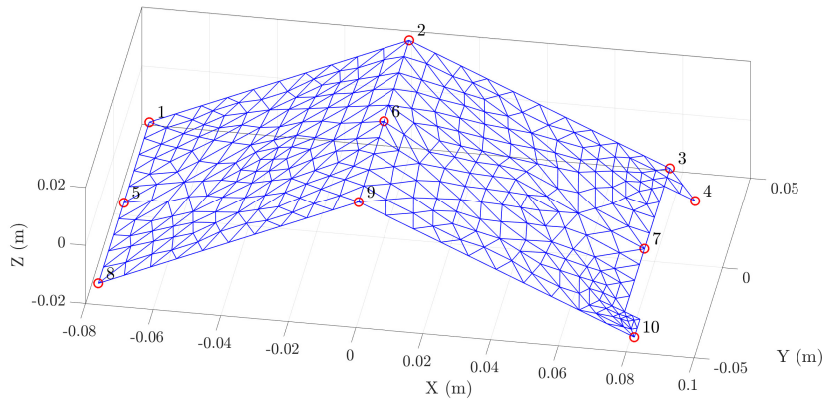

(a)

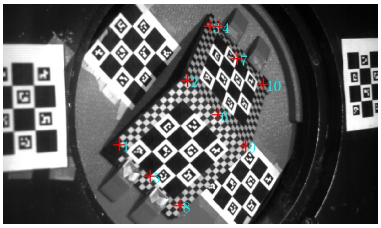

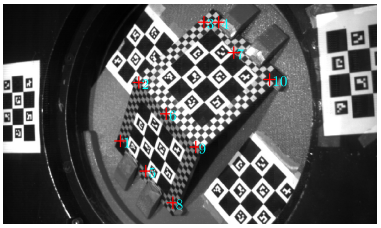

(b) (c)

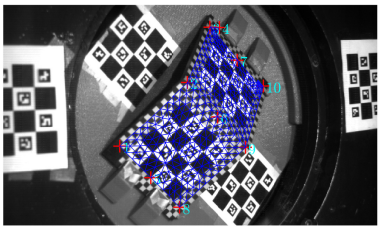

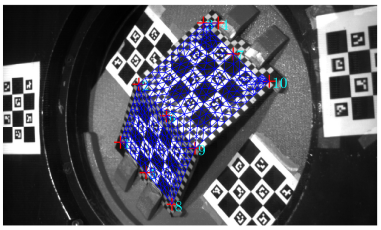

(d) (e)

Fig A.13: Point-to-Point initialization:(a) Virtual FE model of calibration target; selected key points in FE model are plotted as red circles (b)-(c) Hand-selected key points in images for cameras 1 and 2 (d)-(e) Projected FE Mesh (plotted in blue) over the 2D image with the estimated projection matrices for cameras 1 and 2.

610 the 2D images for each camera (Fig A.13d-e.).

611 Finally, as the geometrical relationship between the target and the speci-
612 men is well known, the surface of the laminated glass to be observed is easily
613 calibrated (see Fig 3)

Appendix B. Global S-DIC method

Digital Image Correlation most often relies on the assumption of gray level conservation between a reference image f and a deformed image g, so that for each pixel $\mathbf{x}$

$$f\left(\mathbf{x}, t=0\right) = g\left(\mathbf{x} + \mathbf{u}(\mathbf{x}), t\right) \tag{B.1}$$

where t is the time and $\mathbf{u}$ the pixel displacement. However, this equation is never strictly obeyed due to the presence of acquisition noise, dependence on the camera performances, or subpixel gray-level interpolation error and hence the displacement field is computed from the minimization of the quadratic difference between the two members of Eq. (B.1).

$$\mathcal{W}(\mathbf{u}) = \|f(.) - g(. + \mathbf{u})\|^2 \tag{B.2}$$

calculated on all pixels of the region of interest (ROI).

The philosophy is similar for global S-DIC with multiple view system, but minimization is performed for the 3D displacements and considering all the N_c cameras at once (Hild and Roux 2012; Dufour et al. 2015b; Berny 2020) (in our case $N_c = 2$). The minimization problem, described in equation (2), finally consists of successive corrections of the displacement field from a system assembled from the sum over all cameras of their contribution to the global residual of global stereo-Digital Image Correlation. It is worth emphasizing that the measured displacement is directly the 3D nodal displacement field, minimizing the camera contribution (*i.e.*, residuals for each camera) simultaneously.

The S-DIC measurements presented thereafter are also regularized by a Tikhonov regularization to solve this poorly conditioned problem (Tikhonov

and Arsenin 1977). The minimization problem becomes

$$\left(\sum_{c=1}^{N_c}[\mathbf{H}]^c + \lambda[\mathbf{I}]\right)\cdot\{\delta\mathbf{U}\} = \sum_{c=1}^{N_c}\{\mathbf{b}\}^c + \lambda\left(\{\mathbf{U}_0\} - \{\mathbf{U}\}\right) \tag{B.3}$$

with $[\mathbf{I}]$ the identity matrix, $\mathbf{U}$ the current corrected displacement and $\mathbf{U}_0$ the estimated displacement for this iteration. The weight λ associated to the Tikhonov regularization is chosen as

$$\lambda = 10^{-2}\cdot\lambda_{max} \tag{B.4}$$

with λ_{max} the largest eigenvalue of the S-DIC Hessian matrix $\sum_{c=1}^{N_c}[\mathbf{H}]^c$.

As a remark, the Tikhonov regularization is no longer used when the axisymmetric formulation (section 3) is chosen.

References

C. Alter, S. Kolling, and J. Schneider. An enhanced non–local failure criterion for laminated glass under low velocity impact. *International Journal of Impact Engineering*, 109:342–353, 2017. ISSN 0734-743X. DOI: 10.1016/j.ijimpeng.2017.07.014.

S.C. Angelides, J.P. Talbot, and M. Overend. The effects of high strain-rate and in-plane restraint on quasi-statically loaded laminated glass: a theoretical study with applications to blast enhancement. *Glass Structures & Engineering*, 4(3):403–420, 2019. DOI: 10.1007/s40940-019-00107-4.

S.C. Angelides, J.P. Talbot, and M. Overend. High strain-rate effects from blast loads on laminated glass: An experimental investigation of the post-fracture bending moment capacity based on time–temperature mapping of interlayer yield stress. *Construction and Building Materials*, 273:121658, 2021. ISSN 0950-0618. DOI: 10.1016/j.conbuildmat.2020.121658.

S.C. Angelides, J.P. Talbot, and M. Overend. The influence of fracture pattern on the residual resistance of laminated glass at high strain-rates: an experimental investigation of the post-fracture bending moment capacity based on time-temperature mapping of interlayer yield stress. *Glass Structures & Engineering*, 7(4):549–568, 2022. DOI: 10.1007/s40940-022-00168-y.

B. Beaubier, K. Lavernhe Taillard, G. Besnard, S. Lavernhe, F. Hild, and S. Roux. CAD-based Calibration of a 3D DIC System. In *SEM XII International Congress & Exposition on Experimental and Applied Me-*

chanics, United States, 2012. URL https://hal.archives-ouvertes.fr/hal-00727879.

M. Berny. *High-temperature tests for ceramic matrix composites : from full-field regularised measurements to thermomechanical parameter identification*. Theses, Université Paris-Saclay, 2020. URL https://tel.archives-ouvertes.fr/tel-03204518.

G. Besnard. *Caractérisation et quantification de surfaces par stéréocorrélation pour des essais mécaniques du quasi statique à la dynamique ultra-rapide*. Theses, École normale supérieure de Cachan, 2010. URL https://tel.archives-ouvertes.fr/tel-00538904.

M. Chapelier, R. Bouclier, and J.-C. Passieux. Free-form deformation digital image correlation (FFD-DIC): A non-invasive spline regularization for arbitrary finite element measurements. *Computer Methods in Applied Mechanics and Engineering*, 384:113992, 2021. ISSN 0045-7825. DOI: 10.1016/j.cma.2021.113992.

S. Chen, M. Zang, D. Wang, Z. Zheng, and C. Zhao. Finite element modelling of impact damage in polyvinyl butyral laminated glass. *Composite Structures*, 138:1 – 11, 2016. ISSN 0263-8223. DOI: 10.1016/j.compstruct.2015.11.042.

G. Colantonio, M. Chapelier, R. Bouclier, J.-C. Passieux, and E. Marenic. Non-invasive multilevel geometric regularization of mesh-based 3D shape measurement. *International Journal for Numerical Methods in Engineering*, 121(9):1877–1897, May 2020. DOI: 10.1002/nme.6291.

R. Decourcelle. *Comportement mécanique des vitrages feuilletés sous chargements statiques et dynamiques*. Thesis, Université de Rennes 1, 2011. URL http://www.theses.fr/2011REN1S104.

P. Del Linz, P.A. Hooper, H. Arora, Y. Wang, D. Smith, B.R.K. Blackman, and J.P. Dear. Delamination properties of laminated glass windows subject to blast loading. *International Journal of Impact Engineering*, 105:39–53, 2017. ISSN 0734-743X. DOI: 10.1016/j.ijimpeng.2016.05.015. Design and Analysis of Protective Structures 2015.

J. Dufour, B. Beaubier, F. Hild, and S. Roux. CAD-based Displacement Measurements with Stereo-DIC. *Experimental Mechanics*, 55(9):1657–1668, 2015a. DOI: 10.1007/s11340-015-0065-6.

J. Dufour, F. Hild, and S. Roux. Shape, displacement and mechanical properties from isogeometric multiview stereocorrelation. *The Journal of Strain Analysis for Engineering Design*, 50(7):470–487, 2015b. DOI: 10.1177/0309324715592530.

P. Elzière. *Laminated glass : dynamic rupture of adhesion*. Thesis, Université Pierre et Marie Curie - Paris VI, September 2016. URL https://hal.archives-ouvertes.fr/tel-01381142.

European Norm. NF EN 356. Glass in building – Safety glazing – Testing and classification of resistance to manual attack, September 2000.

European Norm. NF EN 12600. Glass in building – Pendulum impact – Impact test method and classification for flat glasss, September 2003.

F.A.O. Fernandes, R.J. Alves de Sousa, and M. Ptak. A damage model for the simulation of crack initiation and propagation in automotive windshield laminated glass structures. *International Journal of Crashworthiness*, 26 (4):456–464, 2021. DOI: 10.1080/13588265.2020.1727077.

P. Fourton, K. Piroird, M. Ciccotti, and E. Barthel. Adhesion rupture in laminated glass: influence of adhesion on the energy dissipation mechanisms. *Glass Structures & Engineering*, 5:397–410, 2020. DOI: 10.1007/s40940-020-00136-4.

K. Genovese and D. Sorgente. A morphing-based scheme for large deformation analysis with stereo-DIC. *Optics and Lasers in Engineering*, 104:159–172, 2018. ISSN 0143-8166. DOI: 10.1016/j.optlaseng.2017.06.020.

P. Hála, A. Zemanová, J. Zeman, and M. Šejnoha. Numerical study on failure of laminated glass subjected to low-velocity impact. *Glass Structures & Engineering*, 8(1):99–117, 2023. DOI: 10.1007/s40940-022-00210-z.

F. Hild and S. Roux. Digital image correlation. In *Optical Methods for Solid Mechanics. A Full-Field Approach*, 183-228. P. Rastogi and E. Hack, Wiley-VCH, Weinheim (Germany), 2012. ISBN 978-3-527-41111-5.

P. Hooper. *Blast performance of silicone-bonded laminated glass*. Theses, Imperial College London, 2011. URL https://doi.org/10.25560/6861.

P.A. Hooper, R.A.M. Sukhram, B.R.K. Blackman, and J.P. Dear. On the blast resistance of laminated glass. *International Journal of Solids and Structures*, 49(6):899–918, 2012. ISSN 0020-7683. DOI: 10.1016/j.ijsolstr.2011.12.008.

B. Huang, W. Hu, K. Xu, X. Guan, and W. Lu. Experimental and numerical investigation on glass panel subjected to pendulum impact. *International Journal of Impact Engineering*, 173:104457, 2023. ISSN 0734-743X. DOI: 10.1016/j.ijimpeng.2022.104457.

X. Lai, L. Liu, S. Li, M. Zeleke, Q. Liu, and Z. Wang. A non-ordinary state-based peridynamics modeling of fractures in quasi-brittle materials. *International Journal of Impact Engineering*, 111:130 – 146, 2018. ISSN 0734-743X. DOI: 10.1016/j.ijimpeng.2017.08.008.

H. Leclerc, J. Neggers, F. Mathieu, F. Hild, and S. Roux. *Correli 3.0, [IDDN.FR.001.520008.000.S.P.2015.000.31500]*. Paris (France), 2015.

D. Li, H. Zhang, X. Lei, D. Wei, and D. Li. Three-stage breakage model for laminated glass plate under low-velocity impact. *Ceramics International*, 49(2):2648–2662, 2023. ISSN 0272-8842. DOI: 10.1016/j.ceramint.2022.09.245.

Y. Li, D. Xiong, L. Wang, B. Feng, and J. Xu. Dynamic mechanical behavior and pedestrian safety characteristics of toughened laminated windshield. *Composites Part B: Engineering*, 163:740 – 751, 2019. ISSN 1359-8368. DOI: 10.1016/j.compositesb.2019.01.054.

Q. Ma, L. Wu, and D. Huang. An extended peridynamic model for dynamic fracture of laminated glass considering interfacial debonding. *Composite Structures*, 290:115552, 2022. ISSN 0263-8223. DOI: 10.1016/j.compstruct.2022.115552.

M. Martìn, X. Centelles, A. Solé, C. Barreneche, A.I. Fernández, and L.F. Cabeza. Polymeric interlayer materials for laminated glass: A review. *Construction and Building Materials*, 230:116897, 2020. ISSN 0950-0618. DOI: 10.1016/j.conbuildmat.2019.116897.

M.J. Meyland, R.N.W. Eriksen, and J.H. Nielsen. A modified split-hopkinson pressure bar setup enabling stereo digital image correlation measurements for flexural testing. *International Journal of Impact Engineering*, 173: 104480, 2023. ISSN 0734-743X. DOI: 10.1016/j.ijimpeng.2022.104480.

I. Mohagheghian, Y. Wang, L. Jiang, X. Zhang, X. Guo, Y. Yan, A.J. Kinloch, and J.P. Dear. Quasi-static bending and low velocity impact performance of monolithic and laminated glass windows employing chemically strengthened glass. *European Journal of Mechanics - A/Solids*, 63:165–186, 2017. ISSN 0997-7538. DOI: 10.1016/j.euromechsol.2017.01.006.

I. Mohagheghian, M.N. Charalambides, Y. Wang, L. Jiang, X. Zhang, Y. Yan, A.J. Kinloch, and J.P. Dear. Effect of the polymer interlayer on the high-velocity soft impact response of laminated glass plates. *International Journal of Impact Engineering*, 120:150 – 170, 2018. ISSN 0734-743X. DOI: 10.1016/j.ijimpeng.2018.06.002.

C. Morison. *The resistance of laminated glass to blast pressure loading and the coefficients for single degree of freedom analysis of laminated glass*. Theses, Cranfield University, 2007. URL https://dspace.lib.cranfield.ac.uk/handle/1826/4651.

A.A. Nassr, T. Yagi, T. Maruyama, and G. Hayashi. Experimental investiga-

779 tion on damage and wave propagation of pvb laminated glazing structures
780 under impact loading. *Structures*, 29:966–978, 2021. ISSN 2352-0124. DOI:
781 10.1016/j.istruc.2020.12.003.

782 E. Nourry. *Laminated glass behaviour under perforating impact*. Thesis, Arts
783 et Métiers ParisTech, 2005. URL https://pastel.archives-ouvertes.
784 fr/pastel-00001608.

785 J. Pelfrene, J. Kuntsche, S. Van Dam, W. Van Paepegem, and J. Schnei-
786 der. Critical assessment of the post-breakage performance of blast loaded
787 laminated glazing: Experiments and simulations. *International Jour-*
788 *nal of Impact Engineering*, 88:61–71, 2016. ISSN 0734-743X. DOI:
789 10.1016/j.ijimpeng.2015.09.008.

790 J. Pierré, J.-C. Passieux, and J. Périé. Finite Element Stereo Digital Im-
791 age Correlation: Framework and Mechanical Regularization. *Experimental*
792 *Mechanics*, 57:443–456, 2017. DOI: 10.1007/s11340-016-0246-y.

793 T. Pyttel, H. Liebertz, and J. Cai. Failure criterion for laminated glass
794 under impact loading and its application in finite element simulation. *In-*
795 *ternational Journal of Impact Engineering*, 38(4):252 – 263, 2011. ISSN
796 0734-743X. DOI: 10.1016/j.ijimpeng.2010.10.035.

797 M.A. Samieian, D. Cormie, D. Smith, W. Wholey, B.R.K. Blackman, J.P.
798 Dear, and P.A. Hooper. Temperature effects on laminated glass at high
799 rate. *International Journal of Impact Engineering*, 111:177–186, 2018.
800 ISSN 0734-743X. DOI: 10.1016/j.ijimpeng.2017.09.001.

801 M.A. Samieian, D. Cormie, D. Smith, W. Wholey, B.R.K. Blackman, J.P.
802 Dear, and P.A. Hooper. On the bonding between glass and pvb in lami-
803 nated glass. *Engineering Fracture Mechanics*, 214:504 – 519, 2019. ISSN
804 0013-7944. DOI: 10.1016/j.engfracmech.2019.04.006.

805 M. Schuster, J. Schneider, and T.A. Nguyen. Investigations on the exe-
806 cution and evaluation of the pummel test for polyvinyl butyral based
807 interlayers. *Glass Structures & Engineering*, 5(3):371–396, 2020. DOI:
808 10.1007/s40940-020-00120-y.

809 M. Seshadri, S.J. Bennison, A. Jagota, and S. Saigal. Mechanical response
810 of cracked laminated plates. *Acta Materialia*, 50(18):4477 – 4490, 2002.
811 ISSN 1359-6454. DOI: 10.1016/S1359-6454(02)00255-0.

812 M. Shahriari and H. Saeidi Googarchin. Prediction of vehicle impact speed
813 based on the post-cracking behavior of automotive pvb laminated glass:
814 Analytical modeling and numerical cohesive zone modeling. *Engineering*
815 *Fracture Mechanics*, 240:107352, 2020. ISSN 0013-7944. DOI: 10.1016/
816 j.engfracmech.2020.107352.

817 X. Shao, X. Dai, Z. Chen, Y. Dai, S. Dong, and X. He. Calibration of stereo-
818 digital image correlation for deformation measurement of large engineering
819 components. *Measurement Science and Technology*, 27(12):125010, 2016.
820 DOI: 10.1088/0957-0233/27/12/125010.

821 M.A. Sutton, J. Orteu, and H. Schreier. *Image Correlation for Shape, Mo-*
822 *tion and Deformation Measurements: Basic Concepts,Theory and Appli-*

cations. Springer Publishing Company, Incorporated, 1st edition, 2009. ISBN 0387787461.

A. Tikhonov and V.Y. Arsenin. *Solutions of ill-posed problems*. J. Wiley, 1977.

X. Wang, J. Yang, W.T.A. Chong, P. Qiao, S. Peng, and X. Huang. Post-fracture performance of laminated glass panels under consecutive hard body impacts. *Composite Structures*, 254:112777, 2020. ISSN 0263-8223. DOI: 10.1016/j.compstruct.2020.112777.

X. Wang, X. Huang, J. Yang, X. Hou, Y. Zhu, and D. Xie. Experimental and analytical study on the pre-crack impact response of thick multi-layered laminated glass under hard body impact. *International Journal of Mechanical Sciences*, 206:106613, 2021. ISSN 0020-7403. DOI: 10.1016/j.ijmecsci.2021.106613.

G. Yu, Y. Zheng, B. Feng, B. Liu, K. Meng, X. Yang, H. Chen, and J. Xu. Computation modeling of laminated crack glass windshields subjected to headform impact. *Computers & Structures*, 193:139 – 154, 2017. ISSN 0045-7949. DOI: 10.1016/j.compstruc.2017.08.011.